The Effect of Specific Manufacturing Characteristics on PF ITER Full-Size Joint Performance

Pilar Fernandez Pison, Stefanie A. E. Langeslag, Ignacio Aviles Santillana, Alexander Dimitrijevic, Stefano Sgobba, Yury Ilyin, Fabrice Simon, and Byung Su Lim

***Abstract*—The development of new generation superconducting magnets for fusion research, such as the ITER experiment, is largely based on coils wound from so-called "Cable-In-Conduit" Conductors (CICCs). CICCs consist of various types of stainless steel jackets, densely filled with compacted superconducting strands, which are cooled by supercritical helium. The design of the various magnet systems, and in particular the ITER Poloidal Field (PF) coils, imposes the use of electrical joints to connect unit lengths of the CICCs. The electrical joints are delicate, electrical resistive components, carefully designed to provide efficient high current transfer while avoiding heat generation. The PF joints are subjected to fast varying magnetic fields that induce currents which, combined with the Joule heating in the resistive joints due to transport current, increase the temperature of the helium. Various characteristics, including electrical performance and mechanical behavior, have been addressed in the past in order to optimize manufacturing for satisfactory joint operation. Here an extensive post-mortem characterization of pre-qualification full-size PF joints is reported. Void fraction, twist pitch, and the current path connection are investigated in order to understand their effect on electrical performance and tune the manufacturing processes.**

***Index Terms*—Joints, ITER, PF coil, superconducting coils.**

I. Introduction

THE ITER Poloidal Field (PF) magnet system consists of six ring coils based on NbTi superconducting Cable-in-Conduit Conductors (CICCs) [1]. The PF coil system is responsible for the plasma shaping in the Tokamak and contributes to its stability [2]. For that purpose, it provides pulsed magnetic fields with fast varying coil currents [3].

Due to the long length of the conductor required for the coils and manufacturing limitations, the use of electrical joints is necessary to connect unit lengths of CICCs [3]. The electrical joints have been carefully designed to achieve an efficient transfer of high current while avoiding excessive heating which could lead to a degradation in conductor performance [4]. The design is based on the twin-box concept, where two conductor terminations, each made of a stainless steel-Cu explosion-bonded box, are soldered together forming the electrical connection (Fig. 1) [5]. The soldering of the two adjacent Cu-soles of the boxes is done with a shim in between in order to mitigate assembly tolerances [6]; it provides two sole-to-shim contacts which we refer to as sole-to-sole contact. Furthermore, in order to provide additional mechanical strength, the cable strands in direct contact with the Cu-sole are also soldered to it, providing a strand-to-sole contact [6].

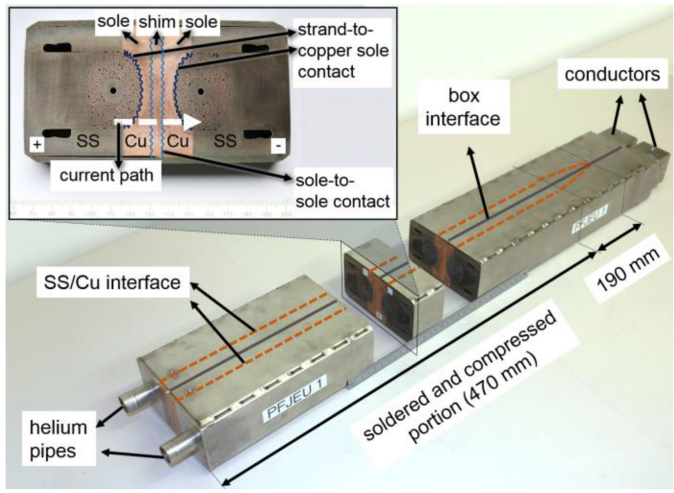

Fig. 1. "Praying hand" PF joint with a slice cut from the middle allowing an internal view of the cross-section. The entire joint is covered by steel compression plates to support the Lorentz forces [11]. The interface between the two boxes is indicated by a continuous line along the longitudinal axis of the joint, whereas the interface between the stainless steel and Cu is indicated by a dashed line. In the detailed view of the cross-section of the joint, the current path is shown with a dashed arrow.

The joint's electrical resistance is a critical parameter for the conductor's performance [7] due to Joule heating generated by the transport current [8]. Moreover, the PF coils are subjected to varying magnetic fields which induce eddy currents in the Cu, as well as intra- and inter-cable coupling currents [9], all introducing significant AC losses in the joint [8]. The mechanical behavior of the joint is also important [5] because of the presence of high Lorentz forces [10]. Thus, various manufacturing solutions have been developed prior to the present work in order to optimize the joint's performance [6]. Pre-qualification

Manuscript received October 29, 2018; accepted February 24, 2019. Date of publication March 6, 2019; date of current version March 29, 2019. *(Corresponding author: Pilar Fernandez Pison.)*

P. Fernandez Pison is with the Department of Continuum Mechanics and Structural Analysis, University Carlos III of Madrid, 28911 Madrid, Spain and also with CERN, CH-1211 Genève, Switzerland (e-mail: pilar.fernandez.pison@cern.ch).

S. A. E. Langeslag, I. Aviles Santillana, and S. Sgobba are with CERN, CH-1211 Genève, Switzerland (e-mail: stefano.sgobba@cern.ch).

A. Dimitrijevic was with CERN, CH-1211 Genève, Switzerland. He is now with the Department of Chemical Engineering, University College London, London WC1e 6BT, U.K. (e-mail: alexander.dimitrijevic.13@ucl.ac.uk).

Y. Ilyin, F. Simon, and B. S. Lim are with the ITER Organization, 13067 St. Paul lez Durance, France (e-mail: yury.ilin@iter.org).

Color versions of one or more of the figures in this paper are available online at http://ieeexplore.ieee.org.

Digital Object Identifier 10.1109/TASC.2019.2902175

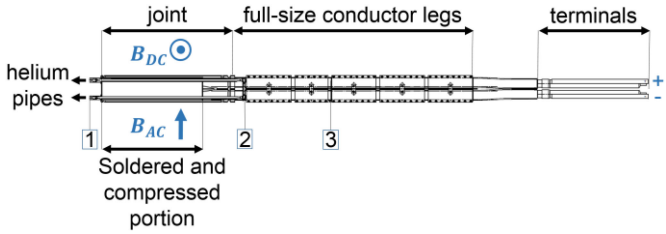

Fig. 2. Schematic view of full-size joint samples named SJ#1 and SJ#2, showing the "positive" current polarity and the direction of the homogeneous DC and AC background fields applied on the entire "soldered and compressed portion" of the joint during the electrical tests. Four voltage taps and two temperature sensors per conductor were used for data measurements. The voltage was measured between the taps on the two conductor legs placed at 40 mm from the joint (Point 2), while the variation of temperature for each conductor was measured by a sensor placed at 490 mm away from the joint (Point 3) and another one placed inside the helium pipes at terminations (Point 1). Courtesy of ASG Superconductors and Fusion for Energy (F4E).

TABLE I
DIFFERENT GEOMETRICAL PARAMETERS OF THE SAMPLES

Parameter	SJ#1	SJ#2
Cu-sole max. thickness[a]	14.6 mm	14.5 mm
Cu-sole min. thickness[b]	6.4 mm	7.9 mm
Strand-to-sole contact length[c]	40.9 mm	36.5 mm
Cu-shim thickness	2.0 mm	7.0 mm

[a]Distance between the SS-Cu and the sole-to-shim interfaces (Fig. 1).
[b]Minimum distance between the strand-to-sole and the sole-to-shim interfaces (Fig. 1).
[c]Total length of the curved strand-to-sole interface for an individual cable within the joint cross-section (Fig. 1).

samples were fabricated for tuning the manufacturing processes and to enable the operators to gain experience for the manufacturing of qualification samples [6].

Here, an extensive characterization of two pre-qualification full-size PF joints is reported, relating their manufacturing characteristics to their electrical performance previously measured in the SULTAN (SUpraLeiter-TestANlage) test facility in the Swiss Plasma Center (SPC) at Villigen, Switzerland.

II. COMPONENTS

The study was performed on two pre-qualification full-size PF joint samples which are identified here as SULTAN joints SJ#1 and SJ#2. A sketch of both samples is shown in Fig. 2. Each sample includes the twin-box joint and two parallel full-size conductor legs connecting via two terminals to the current leads of the SULTAN test facility [11].

The main geometrical differences between the two samples, SJ#1 and SJ#2, are the dimensions of the Cu-sole and shim (Table I). Additionally, Cu-grades of very different purities have been used for the shim and the sole.

III. ELECTRICAL TESTS

The electrical tests carried out at the SULTAN facility included measurements of the joint resistance and of the AC losses. The direction of the DC and AC background fields are shown in Fig. 2. For a "positive" current polarity, the DC field induced normal repulsive Lorentz loads on the boxes, and the AC field induced shear Lorentz loads. In addition, due to the direction of the AC field, the induced currents were forced to flow in planes parallel to the interface of the boxes, generating only eddy currents in the Cu and intra-cable coupling currents.

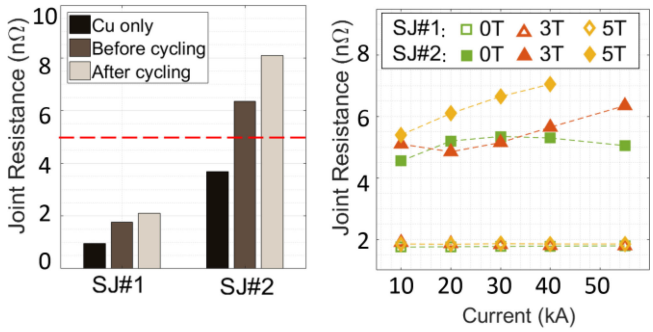

Fig. 3. (a) Joint resistance measurements at a current of 55 kA, 3 T of DC background magnetic field, before and after the loading cycles. Cu-resistance is obtained by simple calculations taking into account the Cu-resistivity (Table II), the geometrical dimensions (Table I and Fig. 1), and the magnetoresistance effect [14]. The maximum acceptable resistance is shown with a dashed line. (b) Evolution of the joint resistance for different DC background magnetic fields and sample current before the loading cycles. Measurement of the resistance of SJ#2 at 5 T and 55 kA was not possible because the sample suffered a quench under these conditions.

A. Joint Resistance Measurement

The resistance of the joints was measured by voltage sensors at a fixed inlet helium temperature of approximately 4.6 K, and mass flow rates of 3 g/s or 10 g/s; using sample currents of 10 kA, 20 kA, 30 kA, 40 kA and 55 kA; in DC background fields of 0 T, 3 T and 5 T. Moreover, in order to study the possible change of the joint resistance with load cycling, the measurements were performed before and after 1000 load cycles carried out at 6 T and −27.5/+27.5 kA.

The acceptance criterion for DC resistance is 5 nΩ at 55 kA and 3 T [6]. For these conditions, the results for both samples are illustrated in Fig. 3(a). SJ#1 fulfilled the criterion maintaining a sufficiently low resistance before and after the loading cycles, whereas SJ#2 already showed an initial joint resistance of 6.4 nΩ suffering a large increase after the loading cycles. Regarding the sensitivity of the resistance with respect to an increase in the current and background magnetic field, SJ#1 showed a stable resistance of around 2 nΩ for all current and field combinations, whereas SJ#2 showed a variation in its resistance (Fig. 3(b)).

B. AC Loss Measurement

Losses were calorimetrically assessed after the loading cycles at a fixed cryogenic temperature of approximately 4.6 K, and 3T background field with a sinusoidal amplitude of 0.2 T.

The results for both samples without any applied current, thus avoiding the contribution of DC losses, are shown in Fig. 4. It is important to note that the PF joints work in 0 Hz to 0.25 Hz diapason with a variation in the magnetic field of approximately 0.4 T/s during 1 s in plasma ignition conditions, which generates the same peak power as the sinusoidal field at 0.16 Hz [12].

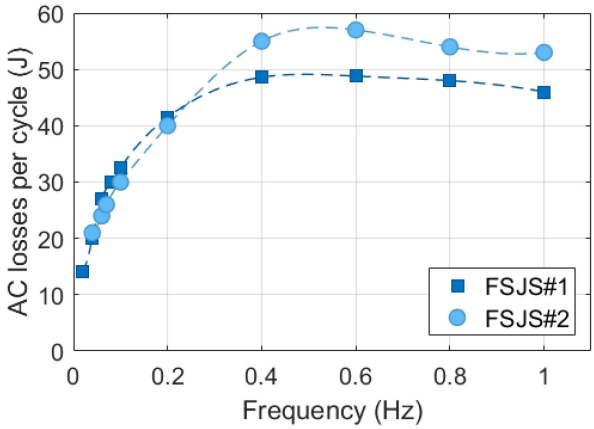

Fig. 4. AC losses per cycle at 3 T background field with a sinusoidal amplitude of 0.2 T without any applied sample current and after the loading cycles.

For low frequencies, and particularly at 0.16 Hz, both samples showed similar AC losses.

IV. Joint Characterization

A test program to characterize the joints was performed at CERN to relate their manufacturing characteristics to their previously measured electrical performance. It includes the measurement of void fraction, twist-pitch angle, Residual Resistivity Ratio (RRR) of the Cu-sole and of the Cu-shim, and verification of the strand-to-sole and sole-to-sole soldering quality.

A. Void Fraction Measurement

Void fraction measurements are performed on stitched images composed of individual images, taken at high magnification, of the cable region. From a stitched image, the cable area is measured and then the void within the cable is quantified based on a color tolerance. The void fraction is thus calculated from the void area over the total cable area. Three measurements per conductor are performed, hence six measurements for each sample. The specimens are extracted from both edges and the center of each sample for statistical reasons. The measurements resulted in a similar void fraction for both samples, with an average and standard deviation of 20.5% $\pm$ 0.3% and 20.0% $\pm$ 0.3% for SJ#1 and SJ#2, respectively. Both samples are in accordance with the design void fraction parameter of 19% $\pm$ 1%.

B. Twist-Pitch Angle Measurement

The strand angle, measured with respect to the longitudinal axis of the joint, gives us an estimation of the twist-pitch angle. This is measured using the strand's imprints on the Cu-sole after their removal. One specimen per conductor is extracted for each sample, and five measurements are performed for each specimen. The measurements showed a similar twist-pitch angle for both samples, 23.4° $\pm$ 1.3° and 25.6° $\pm$ 4.5° for SJ#1 and SJ#2, respectively.

TABLE II
Summary of Cu RRR Measurement

Sample	Resistivity 300 K (nΩ·m)		Resistivity 4.2 K (nΩ·m)		RRR	
	Shim	Sole	Shim	Sole	Shim	Sole
SJ#1	14.22 ± 0.07	14.38 ± 0.20	0.03 ± 0.00	1.94 ± 0.09	421.60 ± 2.72	7.44 ± 0.39
SJ#2	18.08 ± 0.10	22.24 ± 0.28	0.43 ± 0.01	4.57 ± 0.11	42.38 ± 0.60	4.87 ± 0.08

C. RRR Measurement

RRR measurements are performed on specimens with dimensions of approximately 100 mm $\times$ 2 mm $\times$ 2 mm and voltage tap length of 80 mm, as described in [13]. A total of three specimens are extracted from the Cu-shim, and 6 specimens are extracted from one of the Cu-sole for each sample. The summary of the RRR results is shown in Table II, resulting in a RRR for the shim of 421.60 $\pm$ 2.72 and 42.38 $\pm$ 0.60 for SJ#1 and SJ#2, respectively; and a RRR for the sole of 7.44 $\pm$ 0.39 and 4.87 $\pm$ 0.08 for SJ#1 and SJ#2, respectively. The large variation in the results is justified by the different purities used for the Cu of the shim and sole in each sample.

Moreover, from the measured Cu-resistivity values of the shim and sole at 4.2 K without applied field (Table II), we can estimate the resistivity values at 3 T background field taking into account the magnetoresistance effect [14]. This is done for the Cu-shim and sole resistivity for both samples at 4.2 K, in order to facilitate a comparison with the electrical tests. It results in a Cu-shim resistivity of 0.13 nΩ·m $\pm$ 0.00 nΩ·m and 0.50 nΩ·m $\pm$ 0.01 nΩ·m for SJ#1 and SJ#2, respectively; and a Cu-sole resistivity of 2.00 nΩ·m $\pm$ 0.09 nΩ·m and 4.66 nΩ·m $\pm$ 0.11 nΩ·m for SJ#1 and SJ#2, respectively.

D. Assessment of the Strand-to-Sole Soldering Quality

The strand-to-sole soldering characterization is performed four-fold by assessing: the solder thickness between the strands and the Cu-sole, the amount of the strands connected, the percentage of soldered Cu, and the mechanical strength of the bond.

The thickness of the solder is measured by optical techniques on the same specimens used for the void fraction measurement. It resulted in a thickness variation between 120 μm and 718 μm for both conductors of SJ#1, and between 200 μm and 450 μm for SJ#2.

The number of strands connected to the Cu-sole and the percentage of soldered Cu-sole surface are assessed by Computed Tomography (CT) using a ZEISS METROTOM 1500 at 180 kV. For this assessment, a single specimen is extracted from approximately the center of one conductor for each sample. During the post-processing, thirteen equally spaced parallel Y-Z planes (Fig. 5) are analyzed in order to determine the average fraction of connected strands along the length of the specimen. For each plane analyzed, all the first- and second-layer strands are identified, and within them, the number of strands presenting a direct

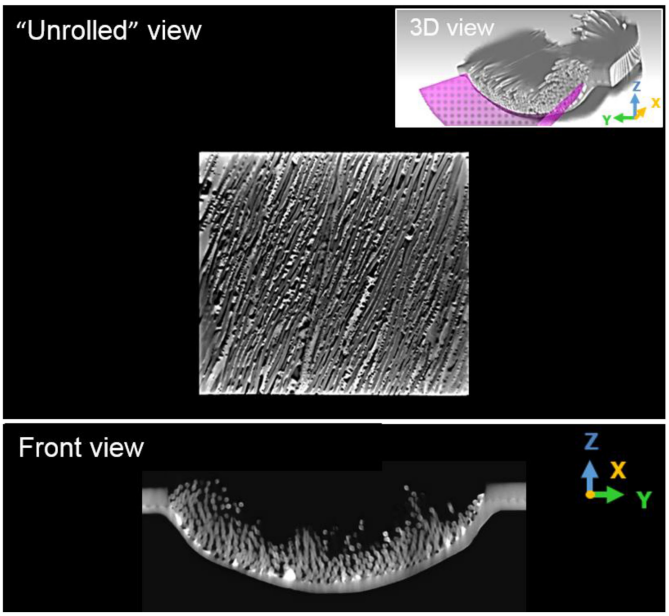

Fig. 5. 3D reconstruction of the CT scan showing the planes of observation used in the post-processing. The "unrolled" view corresponds to the plane presented in the 3-D view, created by a polyline along the strand-to-sole interface. The solder can be identified by bright regions near the Cu-sole, whereas a lack of material is denoted by black regions.

soldering connection with the Cu-sole. The percentage of connected strands is very similar for both samples: the connected first-layer strands resulted in 87.4% $\pm$ 4.9% and 82.7% $\pm$ 7.9% for SJ#1 and SJ#2, respectively; and the connected second-layer strands 30.2% $\pm$ 6.2% and 34.3% $\pm$ 8.4% for SJ#1 and SJ#2, respectively. For the assessment of the fraction of soldered Cu-sole surface, the 3D scan of the specimen is "unrolled" following a polyline along the strand-to-sole interface (Fig. 5). It allows us to obtain a plane parallel to the Cu-sole arc, where a single image can be used to estimate the fraction covered by solder. It resulted in a slightly higher fraction for sample SJ#1 than for SJ#2, 36% compared to 29%, which seems to suggest a better strand-to-sole soldering quality for sample SJ#1 than for SJ#2 based on this analysis. However, this difference comes from the fact that SJ#1 presents some solder not in contact with strands, which in reality do not contribute to the current transfer. Therefore a similar soldering quality can be assumed due to the aforementioned similar percentage of connected strands for both samples.

In order to assess the mechanical strength of the bond, 90° peel-off tests of individual first-layer strands are performed according to [15]. Two specimens per conductor are extracted for each sample to perform the test. Eight strands per specimen, with a bonded length between 10 mm and 20 mm, are peeled off. For both samples, almost all strands showed various high load peaks during the test, which can be related to the intermittent nature of the connection of the superconducting strands to the Cu-sole. The load range was similar for both samples: between 3 N and 8 N. Moreover, the failure mode was predominantly cohesive for both samples.

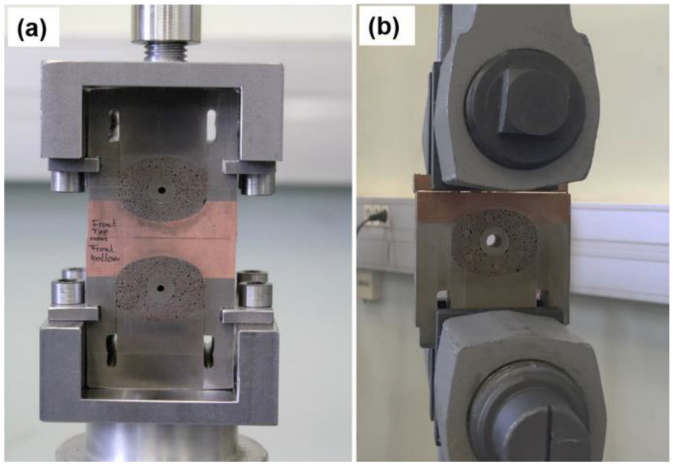

Fig. 6. (a) One of the specimens of SJ#1 during the tensile test, both sole-to-shim interfaces were tested simultaneously. (b) Specimen of SJ#2 during the tensile test where only one sole-to-shim interface was tested.

E. Assessment of the Sole-to-Sole Soldering Quality

The sole-to-sole soldering characterization is performed three-fold by: assessing the overall quality of the solder interfaces by Dye Penetrant Testing (PT), measuring the mechanical strength of the bond by tensile tests, and determining the tensile failure mode by observation of the fracture surfaces.

PT is performed according to the standard ISO 3452-1 along the sample's sole-to-shim interfaces after the removal of the steel compression plates (Fig. 1). SJ#1 showed few indications along the longitudinal length of the interfaces, whereas for SJ#2 linear indications along the entire length were observed for each interface, including severe globular indications in some regions.

The strength of the bond is measured by performing uniaxial tensile tests inspired by the standard ASTM D897 and according to [16]. For SJ#1, three tests were performed on 55 mm long specimens as shown in Fig. 6(a), testing both sole-to-shim interfaces simultaneously. The maximum stress was 7.4 MPa $\pm$ 4.4 MPa. The sample SJ#2 disintegrated during the machining operation to obtain the specimens, revealing the poor state of the bonding. It was only possible to perform a tensile test on a shorter specimen composed of a box bonded to the Cu-shim as shown in Fig. 6(b). The test resulted in a maximum tensile strength of 0.25 MPa.

Observations of the fracture surfaces are carried out after the tensile tests to assess the failure mode. All specimens from SJ#1 showed a cohesive failure with the whole surface covered by solder (Fig. 7(a)). A deeper Scanning Electron Microscopy (SEM) analysis revealed that only some regions were well-bonded and contributed to the tensile strength as described by [17]. These regions feature ductile breakdown and developed dimples when broken by tensile overload. However, other regions were not involved in the fracture and are assumed to be pre-existing discontinuities not affected by the test. Regarding SJ#2, most of the failure was adhesive with a clear lack in soldering substrate on the Cu-shim (Fig. 7(b)).

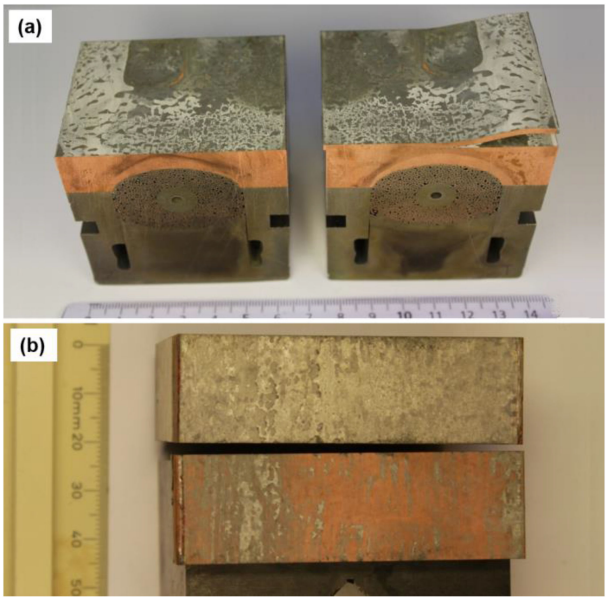

Fig. 7. (a) One of the specimens of SJ#1 after the tensile test. Well-bonded regions have a bright appearance, whereas the discontinuities have a dark appearance. (b) Specimen of SJ#2 after the tensile test, nearly all the Cu-surface of the shim is revealed.

V. Discussion and Conclusion

An extensive characterization was performed on two prequalification full-size PF joint samples, SJ#1 and SJ#2, in order to understand their electrical performance.

A similar void fraction and twist-pitch angle was obtained for both samples, which implies a similar inter-strand contact within the cables. Based on this, it can be inferred that a similar level of intra-cable coupling currents have been induced by the varying magnetic fields, and therefore, a similar contribution to the AC losses have been produced in both samples. Furthermore, the similar inter-strand contact also indicates an equivalent structural support between strands, and therefore a similar degree of local strand movement, induced by Lorentz forces, is expected.

RRR measurements reveal a higher Cu-resistivity of the shim and sole of SJ#2 at 4.2 K, in comparison with SJ#1 (IV.C). This fact, combined with the higher sole and shim thickness and the shorter strand-to-sole contact length (Table I), results in a higher value of the Cu-resistance of SJ#2 compared to SJ#1 (see Fig. 3(a) "Cu only"). Additionally, the Cu-resistivity also influences the AC losses, in particular at low frequencies where the eddy current losses are inversely proportional to the Cu-resistivity and directly proportional to the thickness of components with otherwise equivalent length and width [8]. Thus, for the Cu-shim at a magnetic field of 3 T, the resistivity and the thickness of SJ#2 are each approximately four times higher than in SJ#1 (Table I and IV.C, respectively), these common factors cancel each other out, resulting in similar eddy current losses. Conversely, for the Cu-sole at 3 T, the resistivity of SJ#2 is approximately two times higher than in SJ#1 (IV.C), while the thickness is similar for both samples (Table I); this results in lower eddy current losses for SJ#2. However, the eddy current losses are negligible compared to the cable coupling current losses [18], which consisted of the aforementioned intra-cable coupling currents losses (III). In summary, at 3 T and low frequencies, similar AC losses were generated in both samples, agreeing with the behavior shown in Fig. 4.

Similar strand-to-sole soldering quality was achieved for both samples based on the measured solder thickness, the CT analysis and the peel-off tests. This implies a similar contact resistance at the strand-to-sole interface.

The sole-to-sole contact had a lower quality in SJ#1 than SJ#2 as shown by the PT inspection, the tensile tests and visual observations of the fracture surfaces. Thus, in addition to the aforementioned higher Cu-resistance of SJ#2 compared to SJ#1, the quality of this sole-to-sole contact also contributed to the higher joint resistance of SJ#2 as shown in Fig. 3(a) "Before cycling". The greater increase in resistance after the loading cycles for SJ#2, compared to SJ#1 (see Fig. 3(a) "After cycling"), is explained by the significantly lower strength of the solder bonding of SJ#2 as revealed during the tensile tests. The sole-to-sole solder bonding of SJ#2 could not properly withstand the forces transmitted to the boxes during the loading cycles, leading to a considerably higher deterioration in comparison with that suffered by SJ#1, even with the similar intensity of Lorentz forces. Moreover, the unstable resistance of SJ#2 shown in Fig. 3(b) can be explained by fast saturation of the limited areas showing a good solder quality at the sole-to-sole interface, which forces the current to flow through higher resistance regions. Regarding SJ#1, since the sample presented a better quality at this interface, it was considerably less affected by this saturation effect and the sample's resistance remained stable while the sample current and the background magnetic field increased (Fig. 3(b)).

The extensive characterization successfully explains the observed similarities and differences in the electrical performance of both samples. The similar AC losses at low frequencies are explained by similar void fraction and twist-pitch angle; while the difference in joint resistance is explained by dissimilar Cu-resistivity, and soldering quality at the sole-to-sole interface.

Acknowledgment

The authors would like to thank the SPC, CH, for performing the electrical measurements; Microelectronica SA, RO, for performing the CT scans; A. Porret (CERN) for performing the PT, and D. Richter, S. Prunet, and L. Dufay-Chanat (CERN) for performing the RRR measurements. Thanks are also owed to F. Motschmann (CERN) and to S. A. Garner (CERN) for the helpful discussions.

Disclaimer: The views and opinions expressed herein do not necessarily reflect those of the ITER Organization

References

[1] N. Mitchell, A. Devred, P. Libeyre, B. S. Lim, and F. Savary, "The ITER magnets: Design and construction status," *IEEE Trans. Appl. Supercond.*, vol. 22, no. 3, Jun. 2012, Art. no. 4200809.

[2] M. Huguet *et al.*, "Key engineering features of the ITER-FEAT magnet system and implications for the R&D program," *Nuclear Fusion*, vol. 41, no. 10, pp. 1503–1513, Oct. 2001.

[3] F. Simon, Y. Ilyin, B. S. Lim, F. Cau, R. Herzog, and B. Stepanov, "Reliability considerations for the ITER poloidal field coils," *IEEE Trans. Appl. Supercond.*, vol. 20, no. 3, pp. 423–426, Jun. 2010.

[4] P. Decool, "*Joints for Superconducting Magnets*," Cadarache, France: MATEFU Training School, CEA, Apr. 2009. [Online]. Available: http://www-fusion-magnetique.cea.fr/matefu/school_2/Wednesday/decool-joints.pdf

[5] B. Lim *et al.*, "Design of the ITER PF Coils," *IEEE Trans. Appl. Supercond.*, vol. 21, no. 3, pp. 1918–1921, Jun. 2011.

[6] Y. Ilyin *et al.*, "Qualification program of lap joints for ITER coils," *IEEE Trans. Appl. Supercond.*, vol. 28, no. 3, Apr. 2018, Art. no. 4201306.

[7] Y. Ilyin *et al.*, "Analysis of ITER PF coil joint design under reference operating scenario," *IEEE Trans. Appl. Supercond.*, vol. 26, no. 4, Jun. 2016, Art. no. 4201305.

[8] D. Ciazynski and A. Martinez, "Electrical and thermal designs and analyses of joints for the ITER PF coils," *IEEE Trans. Appl. Supercond.*, vol. 12, no. 1, pp. 538–542, Mar. 2002.

[9] Y. Ilyin *et al.*, "Simulations of twin-box joints for ITER PF coils," *IEEE Trans. Appl. Supercond.*, vol. 24, no. 3, Jun. 2014, Art. no. 9001905.

[10] A. Nijhuis, Y. Ilyin, W. Abbas, B. ten Haken, and H. H. J. ten Kate, "Change of interstrand contact resistance and coupling loss in various prototype ITER NbTi conductors with transverse loading in the Twente Cryogenic Cable Press up to 40,000 cycles," *Cryogenics*, vol. 44, pp. 319–339, May 2014.

[11] P. Decool *et al.*, "Design and manufacture of a prototype NbTi full-size joint sample for the ITER poloidal field coils," *Fusion Eng. Design*, vol. 66, pp. 1165–1169, Sep. 2003.

[12] Y. Ilyin, "Electrical performance of PF pre-qualification joint samples and conclusions for final design," in *Proc. 6th PF Coils Collaboration Meeting ITER Organization*, La Spezia, Italy, Nov. 2016. Internal Communication.

[13] Z. Charifoulline, "Residual resistivity ratio (RRR) measurements of LHC superconducting NbTi cable strands," *IEEE Trans. Appl. Supercond.*, vol. 16, no. 2, pp. 1188–1191, Jun. 2006.

[14] W. R. Hudson, "Copper magnetoresistance devices as magnetometers," NASA TN D-3536, Washington, DC, USA, 1966.

[15] C. Romero Rodriguez and P. Fernandez Pison, "Internal soldering assessment of a PF full size joint sample," in *Proc. CERN*, Genève, Switzerland, May 2017, [Online]. Available: https://edms.cern.ch/document/1753107/3 Internal Communication.

[16] P. Fernandez Pison and S. A. E. Langeslag, "Sole to shim soldering assessment of a full size joint prequalification sample," in *Proc. CERN*, Genève, Switzerland, May. 2017, [Online]. Available: https://edms.cern.ch/document/1753107/3 Internal Communication

[17] P. Ortega Toledano, "Characterization of the Brazing between Two Poloidal Field Boxes for the Tokamak of the ITER Project," Master thesis, Univ. Carlos III of Madrid, Spain, Sep. 2018.

[18] J. Huang, T. Bagni, Y. Ilin, and A. Nijhuis, "Quantitative analysis of electrical and thermal stability of ITER NbTi PF joints," in *Proc. Appl. Supercond. Conf. (ASC)*, Seattle, WA, USA, Oct. 2018.